Published in final edited form as:
Annu Res Br. 2017 January ; 2017: 257–270.

Convergence of large-eddy simulation in the outer region of wall-bounded turbulence

A. Lozano-Durán, **H. J. Bae**

1. Motivation and objectives

Most turbulent flows cannot be calculated by direct numerical simulation (DNS) of the Navier-Stokes equations because the range of scales of motions is so large that the computational cost becomes prohibitive. In large-eddy simulation (LES), only the large eddies are resolved and the effect of the small scales on the larger ones is modeled through a subgrid scale (SGS) model. This process enables a reduction of the computational cost by several orders of magnitude.

Given that the accurate representation and prediction of turbulence is needed in many engineering and scientific applications, validation of SGS models must be considered a task of paramount importance. In particular, the analysis must be framed in the context of a convergence study, which is the cornerstone of validation in computational fluid dynamics. In addition, the grid requirements must be determined for LES to be deemed as a cost-saving approach when compared to DNS. Common benchmark solutions for LES are simple hydrodynamic cases such as forced or decaying isotropic turbulence (Métais & Lesieur 1992), spatial or temporal mixing layers (Vreman *et al*. 1996, 1997) and plane turbulent channel flow (Piomelli *et al*. 1988; Germano *et al*. 1991; Chung & McKeon 2010), among others. See Bonnet *et al*. (1998) for an overview of LES validation.

Most SGS models assume that the effective filter cutoff lies within the inertial range, and the Reynolds number and grid resolutions must comply with this requirement in order to faithfully assess the performance of the models. In unbounded flows, like isotropic turbulence, LES can be computed at relatively coarse grid resolutions while still meeting this condition. However, this is not the case in the logarithmic region of wall-bounded flows, where the energy-containing eddies have sizes proportional to the distance to the wall (Jiménez 2012; Larsson *et al*. 2016). In this case, the LES grid must be accordingly reduced in all directions, increasing the computational cost. This approach is known as wall-resolved LES (WRLES) and can be achieved, for example, through nested grids (Sullivan *et al*. 1996) such as the one depicted in Figure 1. Actual WRLES are scarce, and typically, only the wall-normal resolution is properly refined according to the size of the energy-containing eddies, while the wall-parallel directions remain under-resolved. The grid requirements become more restrictive in the buffer layer, where the viscous effects are non-negligible. If the near-wall grid resolution does not suffice to capture the energy-containing eddies, most SGS models perform poorly (Jiménez & Moser 2000).

The consequence is that the majority of validation studies in turbulent channel flows are WRLES and, hence, their Reynolds numbers tend to be relatively low to make the

computational cost affordable (Choi & Moin 2012). However, it is not clear whether the SGS models are active enough at these low Reynolds numbers to adequately measure their performance. In order to test higher Reynolds numbers without the burden of the wall, a possible solution is the implementation of wall models that act as a surrogate of the near-wall dynamics, or the wall-less channel flow proposed by Lozano-Durán & Bae (2016). Note that turbulent free shear flows such as mixing layers, jets, and wakes are also good candidates in terms of studying shear flows away from the wall. However, their large scales are linearly unstable and sensitive to initial conditions in contrast to the typical wall-bounded flows. In this brief, we assess the convergence of SGS models in the outer region of wall-bounded flows without the effect of the walls. For this purpose, we will employ the two methods proposed above, that are, supplying the correct stress at the wall, or suppressing the near-wall dynamics by a wall-less channel flow.

The present brief is organized as follows. In Section 2, we demonstrate the necessity of wall models before SGS models in LES. We discuss the methodology and the numerical setup to assess the convergence of SGS models in Section 3. The results are shown in Section 4 in terms of the error in the mean velocity profile. We also discuss the difficulties of comparing fluctuating velocities in LES and DNS. Finally, conclusions are given in Section 5.

2. The necessity of wall models before SGS models in LES

To illustrate the poor performance of SGS models when the near-wall region is under-resolved, Figure 2 shows the mean streamwise velocity profile, $\langle \bar{u}_1 \rangle$, for a turbulent channel flow as function of the wall-normal distance x_2, where $\langle \cdot \rangle$ denotes average in homogeneous directions and time, and $(\bar{\cdot})$ is the filtering operation for LES. The details of the simulations are discussed in Section 3.2 (see Table 1), but for now, it is only important to remark that all cases were computed using identical grids (with 13 points per boundary layer thickness, δ) and friction Reynolds number, $Re_\tau \approx 950$. The worst prediction (squares) is obtained from a coarse DNS (no SGS model and no wall model). Ideally, a perfect SGS model will supply the missing stresses at all distances from the wall. Indeed, Figure 2 shows that the solution improves by introducing an SGS model (circles); however, the performance is still poor and $\langle \bar{u}_1 \rangle$ is far from the reference DNS velocity profile. contrast, the agreement with DNS is excellent when the equilibrium wall model from Kawai & Larsson (2012) is applied (triangles), despite the fact that there is no explicit SGS model in this case (although the numerical errors act as an implicit one).

Note that for all cases, the shape of $\langle \bar{u}_1 \rangle$ is barely affected and always very close to the DNS mean velocity profile, even when there is no SGS model. The main source of error comes from the inaccurate prediction of the wall friction velocity, u_τ, that translates into a vertical shift of $\langle \bar{u}_1 \rangle$. This suggests that the application of a SGS model alone is not sufficient to provide the correct stress at the wall, and only by means of a wall model can the problem be attenuated. The result highlights the rarely mentioned fact that, for increasing Re or coarsening of grid resolutions, wall models are needed before SGS models, at least regarding prediction of the mean velocity profile. The rationale behind this requirement is simple: the energy-containing eddies are smaller as they get closer to the wall, and without

any *a-priori* knowledge of the flow or without the necessary computational power, near-wall layer is the first region to become under-resolved.

The problem would be alleviated by performing true WRLES with three-dimensional refinement as the grid approaches the wall. However, this is a quite uncommon practice, and most WRLES suffer at some degree from the same limitation demonstrated in Figure 2. Therefore, it is important to emphasize that, in wall-bounded flows, the testing and validation of SGS is contaminated by the errors accumulated near the wall and many of the mismatches of mean velocity profiles in DNS and LES reported in the literature are probably caused by the necessity of wall models before an SGS model. It is necessary to remark that we do not avocate for LES without a SGS model, but we only underline the fact that validation at low Reynolds number could be meaningless due to inactive SGS models far from the wall and the predominance of the near-wall errors.

3. Benchmarks for the outer region of wall-bounded turbulence

We have acknowledged in Section 2 the necessity of benchmarks for wall-bounded turbulence that are independent of the strict near-wall resolution requirements. To attain this goal, we discuss two different approaches, namely, wall-less and exact wall-stress turbulent channel flows.

3.1. Wall-less and exact wall-stress turbulent channel flows

We consider a plane turbulent channel flow with smooth walls and periodic streamwise and spanwise directions. The incompressible Navier-Stokes equations of motion are

$$\frac{\partial u_i}{\partial t} + \frac{\partial u_i u_j}{\partial x_j} = -\frac{1}{\rho}\frac{\partial p}{\partial x_i} + \nu \frac{\partial^2 u_i}{\partial x_j \partial x_j}, \quad \frac{\partial u_i}{\partial x_i} = 0, \tag{3.1}$$

where u_i, $i = 1, 2, 3$ are the streamwise, wall-normal and spanwise velocities, respectively, p is the pressure, ρ is the flow density, and ν is the kinematic viscosity. The three spatial directions are x_i, $i = 1, 2, 3$ and the walls are located at $x_2 = 0$ and $x_2 = 2\delta$.

The first approach presented is the wall-less channel flow (Lozano-Durán & Bae 2016). We define the slip boundary condition with transpiration as

$$u_i|_w = l \left. \frac{\partial u_i}{\partial n} \right|_w, \quad i = 1, 2, 3, \tag{3.2}$$

where n is the wall-normal direction and l is the slip length, assumed to be constant. Note that Eq. (3.2) complies with the symmetries of the channel flow and the impermeability constraint of the wall on average.

The dynamic system consisting of Eq. (3.1) with boundary conditions in Eq. (3.2) is well defined and can be solved by DNS. The resulting data will be used as a benchmark for LES computed using the same slip boundary condition. We will show in Section 3.3 that Eq. (3.2) suppresses the formation of near-wall viscous layers and breaks the linear scaling of eddies close to the wall. Moreover, in the outer layer, the first-order statistics and spectra of this wall-less channel flow match quantitatively those of wall-bounded simulations. Thus, the wall-less channel flow is an excellent candidate to test the performance of SGS models in the outer region of the flow.

The second approach is the exact wall-stress turbulent channel flow. We perform an LES of a channel where the correct a-priori known wall stress is imposed as a Neumann boundary condition,

$$\left.\frac{\partial \bar{u}_1}{\partial n}\right|_w = \frac{\tau_w - \tau_{12}^{SGS}|_w}{\nu}, \tag{3.3}$$

where τ_w is the mean stress at the wall (known from DNS) and τ_{12}^{SGS} is the tangential component of the SGS stress tensor. This is equivalent to a wall-modeled LES (WMLES) where the wall model is assumed to provide the exact stress at the wall. The LES results are then compared with DNS data. Note that, in contrast to the wall-less channel approach, the exact wall-stress method is prone to error from the under-resolved eddies close the wall when the first wall-normal grid point lies within the logarithmic layer (Larsson *et al.* 2016).

3.2. Numerical experiments

We run two sets of LES of a plane turbulent channel for the wall-less (WL) and the exact-wall-stress (EWS) approaches. For the wall-less flow, three reference DNS are also performed.

The simulations are computed with a staggered second-order finite difference (Orlandi 2000) and fractional-step method (Kim & Moin 1985) with a third-order Runge-Kutta time-advancing scheme (Wray 1990). The flow is driven by imposing a constant mean pressure gradient. Periodic boundary conditions are imposed in the streamwise and spanwise directions. For the top and bottom walls, WL cases are computed imposing the slip boundary condition from Eq. (3.2) with $l = 0.1\delta$. The choice is not unique but must be set in outer units and independent of Re_τ, as will be discussed in Section 3.3. We have confirmed by DNS of the WL cases that the mean viscous stress at the wall is less than 10% of the total

stress for the three Reynolds numbers considered. EWS cases are calculated using Eq. (3.3) as the boundary condition at the walls.

The size of the channel for the WL cases is $2\pi\delta\times2\delta\times\pi\delta$ in the streamwise, wall-normal and spanwise directions, respectively. For the EWS cases, the domain is $8\pi\delta\times2\delta\times3\pi\delta$. The grid resolution is denoted as Δ_1, Δ_2, and Δ_3 for the respective spatial directions. All channel flow simulations were run for at least 100 eddy-turnover times, defined as δ/u_τ, after transients.

For the WL cases, the convergence of two SGS models is tested: dynamic Smagorinsky model (DSM) (Germano *et al.* 1991; Lilly 1992) and anisotropic minimum dissipation (AMD) model (Rozema *et al.* 2015). The DSM and AMD model are regarded as representative of eddy viscosity models with and without test filtering, respectively. We use a wide range of grid resolutions ranging from 1/16 to 1/2 of the DNS resolution for three different Reynolds numbers $Re_\tau \approx 550$, 950, and 2000 and compare the results from WL DNS. For the EWS cases, the convergence of DSM as a function of the grid resolution is tested for two different Reynolds numbers $Re_\tau \approx 4200$, and 8000. EWS cases are compared with DNS data from Lozano-Durán & Jiménez (2014) and Yamamoto & Tsuji (2017).

The list of cases used to motivate the topic in Section 2 is given in Table 1. The list of cases that are discussed for the remainder of the paper is given in Tables 2 and 3.

3.3. One-point statistics for wall-less turbulent channel flows

We discuss the first-order statistics for DNS550-WL, DNS950-WL and DNS2000-WL. These are wall-less DNS cases used as benchmarks in the next section.

First, we assess the contribution of the mean tangential stress in Figure 3(a). The values are larger than 90% for all cases and roughly 98% for DNS2000-WL due to the ability of the boundary condition from Eq. (3.2) to generate nonzero u_1u_2 at the wall. The result demonstrates that the viscous stress contribution is less than 10% at all heights, including the near-wall region, and that the trend is decreasing with Re_τ. The observation aligns with our goal of mitigating the previously dominant viscous stress at the wall.

The characteristic flow length-scales of the no-slip and wall-less DNS are plotted in Figure 3(b) along the x_2 direction. The small, intermediate and large scales are represented by the Kolmogorov length-scale $\eta = (\nu^3/\varepsilon)^{1/4}$, the Taylor microscale $\lambda = (15k/\varepsilon)^{1/2}$, and the integral length-scale $L_\varepsilon = (k/3)^{3/2}/\varepsilon$, respectively, where ε is the rate of energy dissipation, $k = \langle u_i' u_i' \rangle$, and $(\cdot)'$ denotes fluctuating quantities (Pope 2000). Note that L_ε and λ drop rapidly to zero as x_2 approaches the wall for the no-slip DNS, whereas they remain roughly constant for the wall-less DNS. Moreover, comparison of L_ε at two Re_τ shows that the integral length-scale collapses in outer units across the entire boundary layer thickness, including close to the wall. These results are of particular importance and can be read as the disruption of the classic inner-units scaling of the energy-containing eddies at the wall.

The mean velocity profiles are shown in Figure 3(c) and compared with the corresponding no-slip DNS counterparts. The no-slip DNS profiles are shifted to match the center-line

velocity of the WL DNS. The root-mean-squared (RMS) velocity fluctuations are plotted in Figure 3(d) for DNS550-WL. A similar behavior of the RMS velocities was observed for DNS950-WL and DNS2000-WL (not shown). Above $x_2 \approx 0.2\delta$, the first-order statistics of the wall-less channel flows match quantitatively those of wall-bounded simulations except for a shift in the mean velocity profile. This is consistent with previous studies indicating that the outer-layer dynamics are relatively independent of the near-wall cycle (Del Álamo *et al.* 2006; Flores & Jiménez 2006; Hwang & Cossu 2011; Mizuno & Jiménez 2013; Jiménez 2013; Lozano-Durán & Jiménez 2014; Dong *et al.* 2017; Cossu & Hwang 2017).

The results above indicate that the outer-layer physics of the wall-less channel flow are similar to those of wall-bounded flows while avoiding both the viscous effects and the wall-normal scaling of the eddies in the vicinity of the wall. Thus, the wall-less channel flow is an excellent candidate to examine the convergence of LES in the outer region of wall-bounded flows.

4. Results

4.1. Convergence of the mean velocity profile in the outer region

The mean velocity profile is the figure of merit for most LES studies. We quantify the error in $\langle \bar{u}_1 \rangle$ as the mass flow difference between WL/EWS-LES and the corresponding DNS in the outer region, defined as $0.2\delta < x_2 < \delta$. The choice excludes the unphysical range $x_2 < 0.2\delta$ for WL cases and aims to bypass the usually under-resolved region for EWS. In particular, the mean velocity profile error is measured as

$$\mathscr{E} = \left[\frac{\int_{0.2\delta}^{\delta} \left(\langle \bar{u}_1 \rangle - \langle u_1^{DNS} \rangle \right)^2 \mathrm{d}x_2}{\int_{0.2\delta}^{\delta} \langle u_1^{DNS} \rangle^2 \mathrm{d}x_2} \right]^{1/2}, \tag{4.1}$$

where u_1^{DNS} is the DNS solution.

First, we discuss the results for WL cases. Figure 4(a) contains the mean velocity profiles for a selection of three cases at $Re_\tau \approx 2000$ with DSM for different grid resolutions. As expected, $\langle \bar{u}_1 \rangle$ converges to $\langle u_1^{DNS} \rangle$ as the grid is refined. The quantitative assessment of the $\mathscr{E}$ is shown in Figure 4(b) as a function of the characteristic grid resolution based on the cell volume, $\Delta = \sqrt[3]{\Delta_1 \Delta_2 \Delta_3}$. The error ranges from 1% to 20% and is bounded by

$$\mathscr{E} \approx \epsilon \Delta / \delta, \tag{4.2}$$

with $\epsilon \in [0.15, 2.5]$, implying an $\mathcal{O}(\Delta)$ dependence on the grid resolution. For a given Δ, the error increases from $Re_\tau \approx 550$ to $Re_\tau \approx 950$, but shows signs of saturation at $Re_\tau \approx 2000$, that may be an indication that $\mathscr{E}$ will remain constant for higher Reynolds numbers. Both DSM and AMD model yield comparable errors. Figure 4(b) also includes a case equivalent to case DSM550-WL-3 but without an explicit SGS model. Surprisingly, the error is comparable to but smaller than for DSM550-WL-3. Other cases without SGS models for various grid resolutions and Reynolds numbers were computed and their accompanying errors were scattered within the range provided by Eq. (4.2) (not shown). This is a symptom that, despite the desirable properties of the wall-less channel flow as a benchmark for LES, the span of Reynolds numbers examined is too low to scrutinize the effect of the SGS models and offer unambiguous conclusions. This motivates the examination of the EWS cases until higher Re_τ are available for the wall-less channel flow.

Figure 5 is analogous to Figure 4, but for the EWS cases. The errors in Figure 5(b) are slightly smaller than those reported in Figure 4(b). In contrast to the WL cases, the errors for the LES without SGS model are discernibly larger than those calculated with DSM. They are roughly constant for the range of grid resolutions tested but increase with Re_τ. For cases with a SGS model, $\mathscr{E} \sim \Delta$ and collapses in outer units for the two Reynolds numbers investigated, implying that $\mathscr{E} \sim Re_\tau^0$ given a perfect wall model. The error with grid refinement saturates at 1%. Only 10 points per δ are enough to predict the mean velocity with less than 3% error.

Finally, we investigate the relevant physical length-scale for scaling the SGS model errors. For this purpose, we define the local-in-x_2 measure of error as

$$\mathscr{E}_l(x_2) = \left(\frac{\int_{x_2-d}^{x_2+d} \left(\langle \bar{u}_1 \rangle - \langle u_1^{DNS} \rangle \right)^2 \mathrm{d}x_2}{\int_{0.2\delta}^{\delta} \langle u_1^{DNS} \rangle^2 \mathrm{d}x_2} \right)^{1/2}, \tag{4.3}$$

where the integration limits, $x_2 \pm \mathrm{d}$, coincide with the grid locations of for $\bar{u}_1$. The integrals in Eqs. (4.1) and (4.3) are approximated with the trapezoidal rule. Different length scales, namely, the Taylor microscale, the Corrsin scale (Corrsin 1958), and the integral length-scale, computed for the reference DNS were tested. The best collapse was found for the integral length-scale and the results for DSM4200-EWS-1,2,3,4 are shown in Figure 6(a). The local error lies below 1% when the grid resolution is at least 0.5 times smaller than $L_{\mathscr{E}}$, and it drastically drops for $\Delta < 0.2 L_{\mathscr{E}}$. Theses ranges should be understood as tentative estimates. The disproportionately large errors for $\Delta/L_{\mathscr{E}} > 1$ correspond to the points at the wall. They are the consequence of a very low contribution of τ_{12}^{SGS} at $x_2 = 0$ and, hence, a very large $\langle \partial \bar{u}_1 / \partial x_2 \rangle$ in order to achieve the target τ_w. The ratio $\Delta/L_{\mathscr{E}}$ is represented in Figure 6(b) as a function of the wall normal distance. Even when only ten points uniformly

distributed along δ are employed, the ratio Δ/L_ε remains below 0.2 for $x_2 > 0.1\delta$, consistent with the accurate predictions of the mean velocity profile reported in Figure 4. Note that, close to the wall, $L_\varepsilon \approx 3^{3/2}\kappa x_2$. Since the third grid point is always at $x_2 = 2\Delta$, then $\Delta/L_\varepsilon \approx 1/(2 \cdot 3^{3/2}\kappa) \approx 0.25$ for the third grid point independently of Δ. Consequently, no improved predictions are expected in $\langle \bar{u}_1 \rangle$ as Δ is refined until the grid resolution reaches the DNS-like regime. It is important to remark that all cases studied here have $\Delta = \Delta_1 = \Delta_2 = \Delta_3$, and the value of Δ is identical for various different interpretations of the characteristic length-scale of the grid. For anisotropic grids, it is unclear which definition of Δ, if any, will yield equivalent conclusions.

4.2. Comparison of root-mean-squared velocity fluctuations in LES and DNS

In the previous section we have measured the errors on $\langle \bar{u}_1 \rangle$ by accepting without question that LES and DNS are directly comparable. The assumption is reasonable if the filtering operation has little impact on the mean of a variable ϕ, that is, $\langle \bar{\phi} \rangle \approx \langle \phi \rangle$. This is probably the case for the mean velocity profile and moderate filter sizes. However, small-scale motions play a non-negligible role on $\langle u_i'^2 \rangle$, casting doubt about how to proceed for a meaningful comparison between LES and DNS. Two approaches are considered.

If LES is formally interpreted by means of a spatial low-pass filter (Deardorff 1970; Leonard 1975), the meaningful quantities to compare are the RMS of the filtered DNS velocities. The main caveat of this approach is that the actual filtering operation is unknown for most LES, and the grid is assumed to act as an implicit filter (Vasilyev *et al.* 1998; Lund 2003). The question then is which filtering operation should be selected. In the present study, a three-dimensional box-filter is used with a filter size equal to the LES grid resolution in each direction.

Another approach for comparing LES and DNS is by considering the subgrid-scale contribution in the LES terms (Carati *et al.* 2001). Assuming $\langle \bar{\phi} \rangle \approx \langle \phi \rangle$,

$$R_{ij}^{DNS} = \langle u_i u_j \rangle - \langle u_i \rangle \langle u_j \rangle \approx \langle \overline{u_i u_j} \rangle - \langle \bar{u}_i \rangle \langle \bar{u}_j \rangle, \tag{4.4}$$

where the diagonal components of R_{ij}^{DNS} are the mean squared DNS velocity fluctuations. For LES, the SGS model contribution must be included,

$$R_{ij}^{LES} = \langle \bar{u}_i \bar{u}_j \rangle + \langle \tau_{ij}^{SGS} \rangle - \langle \bar{u}_i \rangle \langle \bar{u}_j \rangle, \tag{4.5}$$

where $R_{ij}^{DNS} \approx R_{ij}^{LES}$. A limitation of Eq. (4.5) is that for the incompressible Navier–Stokes equations, the subgrid contribution τ_{ij}^{SGS} is usually modeled as a traceless quantity. In order to allow for direct comparison, only the deviatoric contributions of R_{ij}^{DNS} and R_{ij}^{LES} must be taken into consideration (Winckelmans *et al.* 2002). We will denote the traceless counterparts of R_{ij}^{DNS} and R_{ij}^{LES} as R_{ij}^{DNS*} and R_{ij}^{LES*}, respectively. In this manner, LES and DNS stresses are comparable without prescribing a particular filtering operation.

Both approaches are compiled in Figure 7(a) for the streamwise velocity fluctuations. The unfiltered DNS is also plotted for comparison. The best agreement is between LES and filtered DNS, while $R_{11}^{DNS} > R_{11}^{LES}$. However, the surprisingly good agreement between the filtered DNS and LES is not consistent with an actual filtering operation, as evidenced in the one-dimensional premultiplied spectra for cases DSM4200-EWS-2,3,4 at $y = \delta$ (Figure 7b). The spectra show that the streamwise energy component is piled up towards the larger scales as the grid is coarsened, whereas the main expected effect from an actual filter is the reduction of the energy content in the scales below the filter cutoff. The energy in the large scales might increase slightly due to the filtering in the wall-normal direction. However, some tests carried out for filtered DNS and not reported here revealed that this effect is weak.

5. Conclusions

The assessment of the error in SGS models as a function of Reynolds number and grid resolution is a challenging task for LES of wall-bounded flows due to the effect of the wall. We have shown that the main contributor to the mismatch in the mean velocity profile can be attributed to errors in the near-wall region. Given that the current SGS models are known to be deficient near the wall and that true WRLES are uncommon, our results imply that wall models are necessary prior to SGS models for decreasing resolution in wall units. For example, for $Re_\tau \approx 1000$ and 20 points per δ, errors smaller than 1% in the mean velocity profile can be obtained by WMLES without an explicit SGS model.

In order to test the SGS models in the outer region independently of the effect of the wall, we have designed two numerical experiments: wall-less and exact-wall-stress channel flows. In the former, the no-slip boundary condition at the wall is replaced by a slip boundary condition with transpiration. The resulting non-zero Reynolds stresses at the wall eliminates the severe grid resolution requirements characteristic of the no-slip wall. In the latter, the integrated effect of the near-wall region on the outer flow is bypassed by supplying the exact stress at the wall. Both numerical experiments retain the same physics as the traditional channel flow far from the wall.

The main result is that for the two SGS model tested (DSM and AMD model), the LES error in the mean velocity profile scales as the grid resolution in outer units for $Re_\tau > 2000$. Note also that only 10 grid points in δ are enough to predict the mean velocity profile with less than 3% error. When no SGS model is used, the error remains roughly constant for $\Delta/\delta >$

1/40 and increases with Reynolds number. Note that the discussion above applies only to the outer region of the flow.

We have investigated the relevant physical length-scale to measure the performance of SGS models. Errors in the mean velocity profile collapse the best when the grid resolution is expressed in integral length-scale units. Moreover, they remain bounded below 1% when the grid resolves at least 50% of L_{ε}.

Quantification of the errors in terms of the fluctuating velocities is ambiguous. If we assume that the LES equations are formally derived from the filtered Navier–Stokes equations, the turbulence intensities should be compared to the filtered DNS counterparts. A first examination of this hypothesis shows that the LES RMS fluctuations agree reasonably well with the filtered DNS values using a box-filter with filter size equal to the LES grid. However, a detailed examination of the spectra shows that the effect of grid coarsening in LES is inconsistent with a filtering operation. Another alternative was examined by taking into account the SGS contribution and comparing only the deviatoric components of the stresses. The results were still unsatisfactory, implying that the LES RMS velocity fluctuations may have no clear procedence from DNS.

Since we have demonstrated the good performance of two SGS models in predicting the mean velocity profile in the outer region of wall-bounded turbulence, our work emphasizes the importance of WMLES. Future efforts should be devoted to the development and assessment of accurate wall models.

Acknowledgments

This work was supported by NASA under the Transformative Aeronautics Concepts Program, Grant #NNX15AU93A.

REFERENCES

Bonnet J, Moser R & Rodi W 1998 A selection of test cases for the validation of large eddy simulations of turbulent flows. AGARD Rep #345.

Carati D, Winckelmans GS & Jeanmart H 2001 On the modelling of the subgrid-scale and filtered-scale stress tensors in large-eddy simulation. J. Fluid Mech 441, 119–138.

Choi H & Moin P 2012 Grid-point requirements for large eddy simulation: Chapman's estimates revisited. Phys. Fluids 24, 011702.

Chung D & McKeon B 2010 Large-eddy simulation of large-scale structures in long channel flow. J. Fluid Mech 661, 341–364.

Corrsin S 1958 Local isotropy in turbulent shear flow. NACA Res. Memo #58B11.

Cossu C & Hwang Y 2017 Self-sustaining processes at all scales in wall-bounded turbulent shear flows. Phil. Trans. R. Soc. A 375, 20160088. [PubMed: 28167581]

Deardorff J 1970 A numerical study of three-dimensional turbulent channel flow at large Reynolds numbers. J. Fluid Mech 41, 453–480.

Del Álamo JC, Jiménez J, Zandonade P & Moser RD 2006 Self-similar vortex clusters in the turbulent logarithmic region. J. Fluid Mech 561, 329–358.

Dong S, Lozano-Durán A, Sekimoto A & Jiménez J 2017 Coherent structures in homogeneous shear turbulence compared with those in channels. J. Fluid Mech 816, 167–208.

Flores O & Jiménez J 2006 Effect of wall-boundary disturbances on turbulent channel flows. J. Fluid Mech 566, 357–376.

Germano M, Piomelli U, Moin P & Cabot WH 1991 A dynamic subgrid-scale eddy viscosity model. Phys. Fluids A 3, 1760.

Hwang Y & Cossu C 2011 Self-sustained processes in the logarithmic layer of turbulent channel flows. Phys. Fluids 23, 061702.

Jiménez J 2012 Cascades in wall-bounded turbulence. Annu. Rev. Fluid Mech 44.

Jiménez J 2013 Near-wall turbulence. Phys. Fluids 25, 101302.

Jiménez J & Moser RD 2000 Large-eddy simulations: Where are we and what can we expect? AIAA J 38, 605–612.

Kawai S & Larsson J 2012 Wall-modeling in large eddy simulation: Length scales, grid resolution, and accuracy. Phys. Fluids 24, 015105.

Kim J & Moin P 1985 Application of a fractional-step method to incompressible Navier-Stokes equations. J. Comp. Phys 59, 308–323.

Larsson J, Kawai S, Bodart J & Bermejo-Moreno I 2016 Large eddy simulation with modeled wall-stress: recent progress and future directions. Mech. Eng. Rev 3, 15–00418.

Leonard A 1975 Energy cascade in large-eddy simulations of turbulent fluid flows. In Turbulent Diffusion in Environmental Pollution (ed. Frenkiel F & Munn R), Adv. Geophys, 18, pp. 237–248.

Lilly DK 1992 A proposed modification of the Germano subgrid-scale closure method. Phys. Fluids A 4, 633–635.

Lozano-Durán A & Bae HJ 2016 Turbulent channel with slip boundaries as a benchmark for subgrid-scale models in LES. Annual Research Briefs, Center for Turbulencee Research, Stanford University, pp. 97–103.

Lozano-Durán A & Jiménez J 2014 Effect of the computational domain on direct simulations of turbulent channels up to $Re_\tau = 4200$. Phys. Fluids 26, 011702.

Lozano-Durán A & Jiménez J 2014 Time-resolved evolution of coherent structures in turbulent channels: characterization of eddies and cascades. J. Fluid Mech 759, 432–471.

Lund TS 2003 The use of explicit filters in large eddy simulation. Comput. Math. App 46, 603–616.

Métais O & Lesieur M 1992 Spectral large-eddy simulation of isotropic and stably stratified turbulence. J. Fluid Mech 239, 157–194.

Mizuno Y & Jiménez J 2013 Wall turbulence without walls. J. Fluid Mech 723, 429–455.

Orlandi P 2000 Fluid Flow Phenomena: A Numerical Toolkit Springer.

Piomelli U, Moin P & Ferziger JH 1988 Model consistency in large eddy simulation of turbulent channel flows. Phys. Fluids 31, 1884–1891.

Pope SB 2000 Turbulent Flows Cambridge University Press.

Rozema W, Bae HJ, Moin P & Verstappen R 2015 Minimum-dissipation models for large-eddy simulation. Phys. Fluids 27, 085107.

Sullivan PP, McWilliams JC & Moeng C-H 1996 A grid nesting method for large-eddy simulation of planetary boundary-layer flows. Bound.-Lay. Meteorol 80, 167–202.

Vasilyev OV, Lund TS & Moin P 1998 A general class of commutative filters for les in complex geometries. J. Comp. Phys 146, 82–104.

Vreman B, Geurts B & Kuerten H 1996 Large-eddy simulation of the temporal mixing layer using the clark model. Theor. Comp. Fluid Dyn 8, 309–324.

Vreman B, Geurts B & Kuerten H 1997 Large-eddy simulation of the turbulent mixing layer. J. Fluid Mech 339, 357–390.

Winckelmans G, Jeanmart H & Carati D 2002 On the comparison of turbulence intensities from large-eddy simulation with those from experiment or direct numerical simulation. Phys. Fluids 14, 1809–1811.

Wray AA 1990 Minimal-storage time advancement schemes for spectral methods. Unpublished report, NASA Ames Research Center.

Yamamoto Y & Tsuji Y 2017 Effects of large-scale structures on inner layer in high reynolds number turbulent channel flow. In 10th International Symposium on Turbulence and Shear Flow Phenomena (TSFP-10).

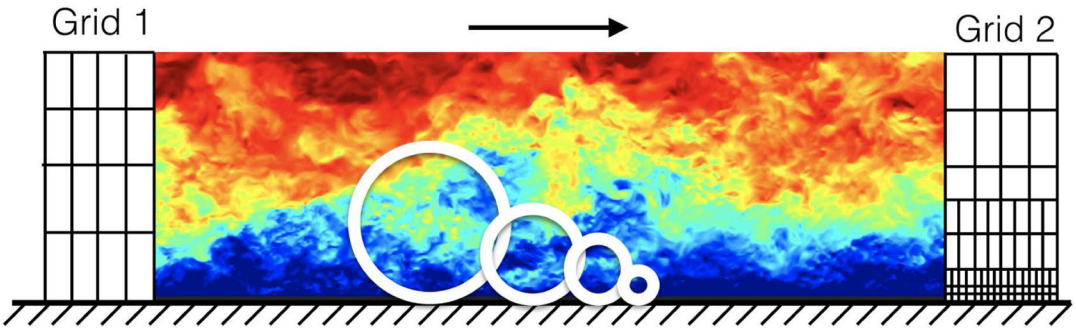

Figure 1.

Instantaneous streamwise velocity contours of a turbulent channel flow and sketch of wall-attached eddies of different sizes (white circles). Grid 1 (left) depicts a uniform grid typical of WMLES. Grid 2 (right) is a nested grid necessary for WRLES.

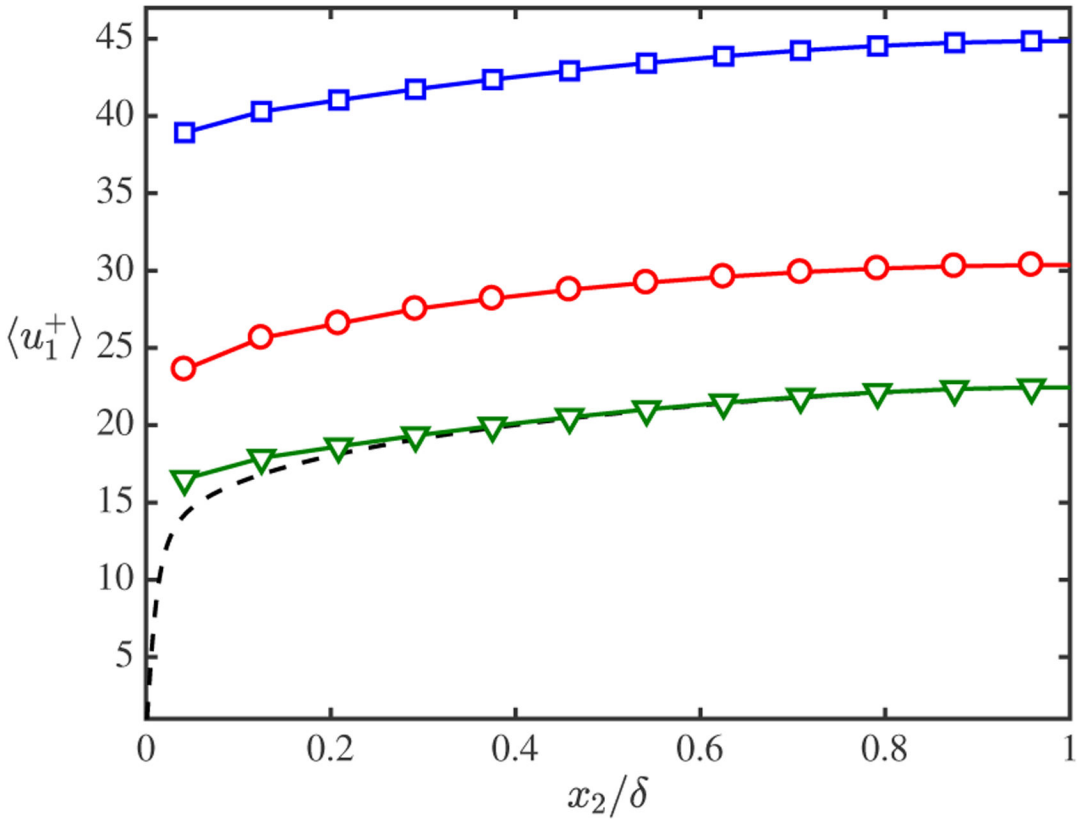

Figure 2.
Mean streamwise velocity profile. The cases plotted are NM950-NS-1 (squares), DSM950-NS-1 (circles), and NM950-EQWM-1 (triangles). DNS is dashed line.

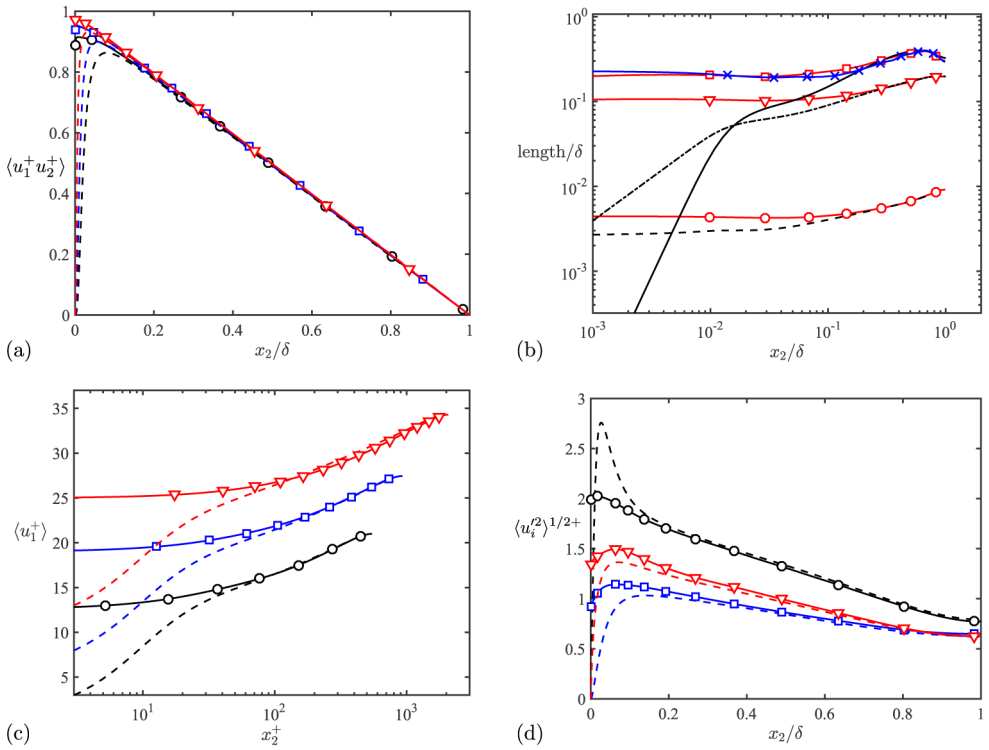

Figure 3.

(a) Mean tangential Reynolds stress for DNS550-WL (circles), DNS950-WL (squares), and DNS2000-WL (triangles). Corresponding dashed lines are no-slip DNS. (b) Kolmogorov length-scale (no-slip DNS, dashed line; DNS550-WL, circles), Taylor microscale (no-slip DNS, dot-dashed line; DNS550-WL, triangles), and integral length-scale (no-slip DNS, solid line; DNS550-WL, squares; DNS950-WL, crosses). (c) Mean velocity profile for DNS550-WL (circles), DNS950-WL (squares), and DNS2000-WL (triangles). The profiles for DNS950-WL and DNS2000-WL are shifted 5 and 10 wall units, respectively, in the vertical direction for clarity. Dashed lines are corresponding no-slip DNS adjusted to match the center-line velocity of the WL cases. (d) Streamwise (circles), wall-normal (squares), and spanwise (triangles) RMS velocity fluctuations for DNS550-WL. Corresponding dashed lines are no-slip DNS.

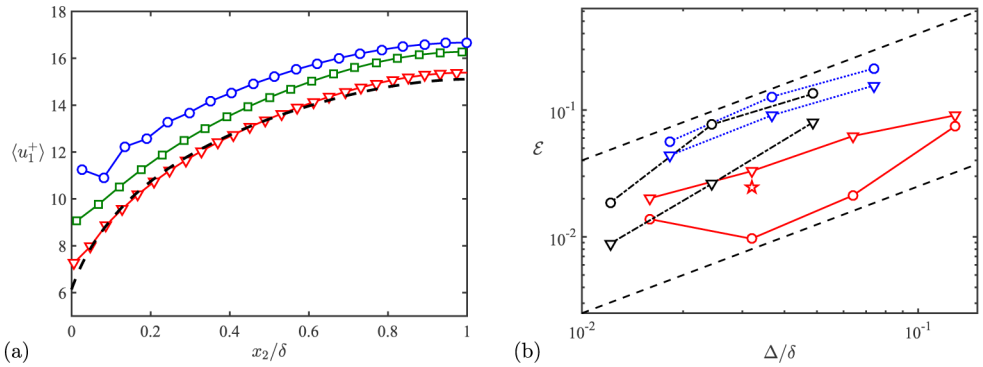

Figure 4.

(a) Mean streamwise velocity profile for DSM2000-WL-1 (circles), DSM2000-WL-2 (squares) and DSM2000-WL-3 (triangles). Dashed line is DNS2000-WL. (b) Error in the mass flow given as a function of grid resolution for two SGS models, DSM (circles) and AMD model (triangles), and no SGS model (pentagram). $Re_\tau \approx 550$, solid lines; 950, dotted lines; and 2000, dot-dashed lines. Dashed lines are $\mathscr{E} = 0.15\Delta/\delta$ and $2.5\Delta/\delta$.

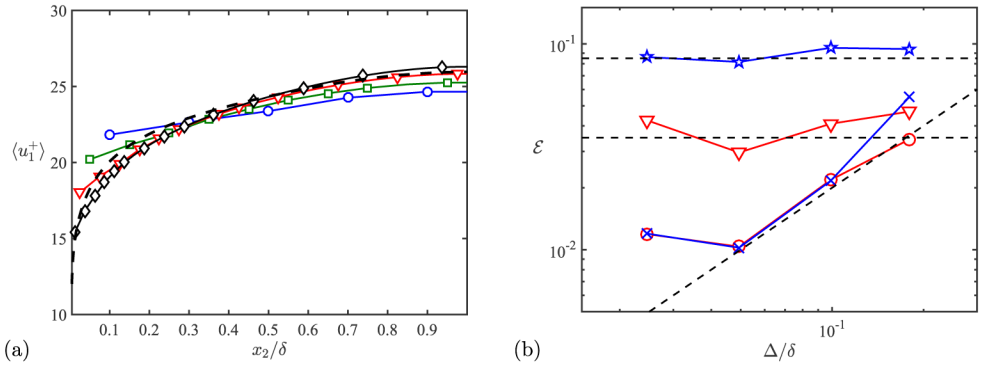

Figure 5.

(a) Mean streamwise velocity profile for DSM4200-EWS-1 (circles), DSM4200-EWS-2 (squares), DSM4200-EWS-3 (triangles), and DSM4200-EWS-4 (diamonds). DNS is dashed line. (b) Error in mass flow as a function of grid resolution. DSM4200-EWS, circles; DSM8000-EWS, crosses; NM4200-EWS, triangles; and NM8000-EWS, pentagrams. Dashed lines are $\mathscr{E} = 0.2\Delta/\delta$, 0.035 and 0.085.

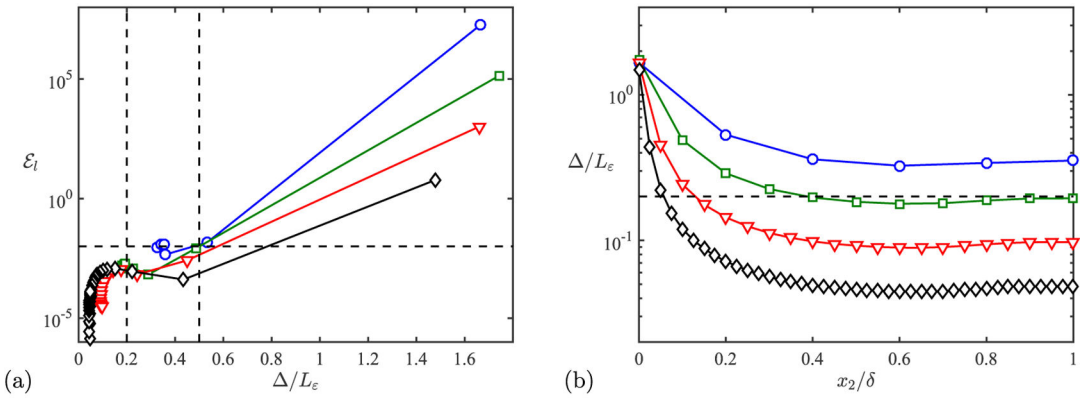

Figure 6.

(a) Local error as a function of the grid size in integral length-scale units. Dashed lines are $\mathscr{E}_l = 10^{-2}$, $\Delta = 0.8L_\varepsilon$ and $\Delta = 0.2L_\varepsilon$. (b) Grid size in integral length-scale units as a function of the wall-normal direction. The dashed line is $\Delta = 0.2L_\varepsilon$. DSM4200-EWS-1 (circles), DSM4200-EWS-2 (squares), DSM4200-EWS-3 (triangles), and DSM4200-EWS-4 (diamonds).

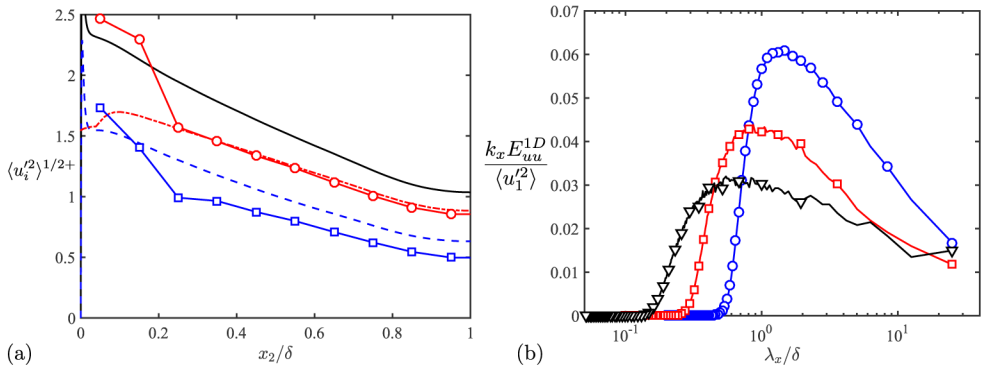

Figure 7.

(a) Streamwise RMS fluctuations for $Re_\tau \approx 4200$. DNS, solid line; filtered DNS, dot–dashed line; DSM4200-EWS-2, circles; R_{11}^{DNS*}, dashed line; R_{11}^{LES*}, squares. (b) Premultiplied streamwise energy spectra as a function of the streamwise wavelength for DSM4200-EWS-2 (circles), DSM4200-EWS-3 (squares), and DSM4200-EWS-4 (triangles).

Table 1.

Tabulated list of cases used in Section 2.

Case	Wall condition	Re_τ	Δ_1/δ	Δ_2/δ	Δ_3/δ	SGS model
NM950-NS-1	NS					NM
DSM950-NS-1	NS	950	0.10	0.080	0.050	DSM
NM950-EQWM-1	EQWM					NM

Table 2.

Tabulated list of cases for WL simulations.

Case	Wall condition	Re_τ	Δ_1/δ	Δ_2/δ	Δ_3/δ	SGS model
DNS550-WL	WL	550	0.012	0.0067	0.0061	N/A
DNS950-WL		950	0.0061	0.0050	0.0031	
DNS2000-WL		2000	0.0041	0.0033	0.0020	
DSM550-WL-1	WL	550	0.20	0.10	0.10	DSM
DSM550-WL-2			0.10	0.050	0.050	
DSM550-WL-3			0.050	0.025	0.025	
DSM550-WL-4			0.025	0.012	0.012	
DSM950-WL-1	WL	950	0.10	0.080	0.050	DSM
DSM950-WL-2			0.050	0.040	0.025	
DSM950-WL-3			0.025	0.020	0.012	
DSM2000-WL-1	WL	2000	0.065	0.052	0.032	DSM
DSM2000-WL-2			0.032	0.026	0.016	
DSM2000-WL-3			0.016	0.013	0.0082	
AMD550-WL-1	WL	550	0.20	0.10	0.10	AMD
AMD550-WL-2			0.10	0.050	0.050	
AMD550-WL-3			0.050	0.025	0.025	
AMD550-WL-4			0.025	0.012	0.012	
AMD950-WL-1	WL	950	0.10	0.080	0.050	AMD
AMD950-WL-2			0.050	0.040	0.025	
AMD950-WL-3			0.025	0.020	0.012	
AMD2000-WL-1	WL	2000	0.065	0.052	0.032	AMD
AMD2000-WL-2			0.032	0.026	0.016	
AMD2000-WL-3			0.016	0.013	0.0082	

Table 3.

Tabulated list of cases for EWS simulations.

Case	Wall condition	Re_τ	Δ_1/δ	Δ_2/δ	Δ_3/δ	SGS model
NM4200-EWS-1	EWS	4200	0.20	0.20	0.20	NM
NM4200-EWS-2			0.10	0.10	0.10	
NM4200-EWS-3			0.050	0.050	0.050	
NM4200-EWS-4			0.025	0.025	0.025	
DSM4200-EWS-1	EWS	4200	0.20	0.20	0.20	DSM
DSM4200-EWS-2			0.10	0.10	0.10	
DSM4200-EWS-3			0.050	0.050	0.050	
DSM4200-EWS-4			0.025	0.025	0.025	
NM8000-EWS-1	EWS	8000	0.20	0.20	0.20	NM
NM8000-EWS-2			0.10	0.10	0.10	
NM8000-EWS-3			0.050	0.050	0.050	
NM8000-EWS-4			0.025	0.025	0.025	
DSM8000-EWS-1	EWS	8000	0.20	0.20	0.20	DSM
DSM8000-EWS-2			0.10	0.10	0.10	
DSM8000-EWS-3			0.050	0.050	0.050	
DSM8000-EWS-4			0.025	0.025	0.025	